Materials Chemistry and Physics 262 (2021) 124301

Contents lists available at ScienceDirect

Materials Chemistry and Physics

journal homepage: www.elsevier.com/locate/matchemphys

Synthesis of $NiMoO_4$ ceramics by proteic sol-gel method and investigation of their catalytic properties in hydrogen production

Maíra V. da Silva [a], Humberto V. Fajardo [a], Thenner S. Rodrigues [b], Felipe A. e Silva [b], Vanderlei S. Bergamaschi [c], Anderson Dias [d], Kisla P.F. Siqueira [a,*]

[a] Department of Chemistry, Laboratory of Ceramic Materials and Raman Spectroscopy, Federal University of Ouro Preto, Campus Morro Do Cruzeiro, ICEB II, 35400-000, Ouro Preto, MG, Brazil
[b] Nanotechnology Engineering Program, Alberto Luiz Coimbra Institute for Graduate Studies and Research in Engineering, COPPE, Federal University of Rio de Janeiro, Av. Horácio Macedo, 2030, 21.941-972, Rio de Janeiro, RJ, Brazil
[c] Nuclear and Energy Research Institute, IPEN-CNEN/SP, Av. Prof. Lineu Prestes, 2242, 05508-000, São Paulo, SP, Brazil
[d] Department of Chemistry, ICEx, Federal University of Minas Gerais, 31270-901, Belo Horizonte, MG, Brazil

HIGHLIGHTS

- $NiMoO_4$ catalysts were prepared by proteic sol-gel method.
- Edible gelatin was used as precursor in the synthesis of the catalysts.
- $NiMoO_4$ were used for hydrogen production from ethanol steam reforming.
- $NiMoO_4$ showed good performance for hydrogen production.

GRAPHICAL ABSTRACT

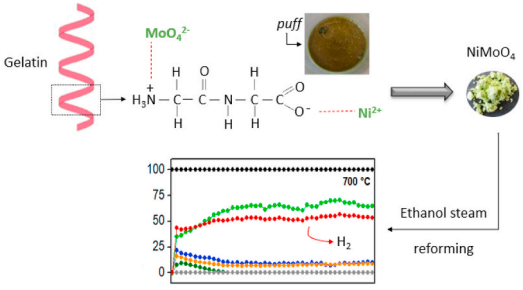

ARTICLE INFO

Keywords:
Hydrogen production
Molybdates
Sol-gel chemistry
Catalytic properties

ABSTRACT

A proteic sol-gel route was used in the production of $NiMoO_4$ catalysts, which used edible gelatin as a precursor. The triple helix structure of a protein in contact with identical structures acquires an unfolded form, which favors the interaction of the reactive groups of the gelatin (NH_3^+ and COO^-) with the metallic ions (MoO_4^{2-} and Ni^{2+}). The synthesized catalysts were thoroughly characterized using techniques such as X-ray diffraction, thermogravimetric and differential thermal analysis, Raman scattering, scanning and transmission electron microscopies, UV–Vis spectroscopy, and colorimetry. The results showed that it is possible to prepare the phase-pure α-$NiMoO_4$ polymorph only at temperatures above 700 °C, while a mixture of the polymorphs α and β were obtained at lower temperatures. The synthesized materials calcined at 300, 500, and 700 °C have their catalytic potentials tested in the ethanol steam reforming reaction aiming the production of hydrogen and presented a good performance. The results indicated that among tested materials, the sample calcined at 700 °C exhibited the highest stability, activity, and best selectivity relative to the product of interest.

* Corresponding author.
E-mail address: kisla@ufop.edu.br (K.P.F. Siqueira).

https://doi.org/10.1016/j.matchemphys.2021.124301
Received 7 November 2020; Received in revised form 16 January 2021; Accepted 19 January 2021
Available online 23 January 2021

1. Introduction

The proteic sol-gel method has been used for the production of ceramic materials by many authors [1–10]. The first study using the protein methodology was made by Macedo et al. [6] using coconut water. Furthermore, because of the high concentration of proteins and sugar in the composition of edible gelatin, Oliveira et al. [7] proposed its use as an organic precursor for obtaining nanometric materials by proteic sol-gel method. This method exhibits some advantages such as high homogeneity besides its ability to produce nanometric particles. Besides, the proteic sol-gel methodology appears to be a relatively simple and low-cost route and does not generate toxic waste; which makes it an environmentally-friendly process [4]. Significant efforts have been made to develop products and processes that are less toxic and aggressive to the environment. Therefore, the proteic sol-gel methodology using edible gelatin becomes a promising processing route for the synthesis of ceramic materials. The gelatin is a favorable substance which is composed basically of protein (84–90%), water (8–12%), and mineral salts (2–4%), as indicated by the merchants of the product.

The proteic sol-gel method is characterized by a variation in the conventional sol-gel method, in which alkoxides are replaced by gelatin [4–8]. Thus, the sol-gel conventional method was adapted so that the synthesis time and energy could be reduced [7,9]. Generally, the synthesis process consists of four stages follows solubilization, the formation of metal chelates, drying, and calcination [4,5,7]. The main difference and advantage of this method over conventional sol-gel is the absence of the polymerization step. Thus, in this case, the polymerization step is replaced by the chain itself formed from the amino acids present in the gelatin structure, which elude the gelatinization process [5–10]. Thereby, the method becomes a simpler proposal, economical, and environmentally safe.

In this work, the edible gelatin was used in the production of $NiMoO_4$ catalysts. Among the metallic molybdates, those of nickel and cobalt have been investigated widely due to their catalytic, magnetic, luminescent, and electric properties [11–20]. Here, $NiMoO_4$ was used as a catalyst in the ethanol steam reforming (ESR) for hydrogen production. Hydrogen is now considered as the future fuel given the abundance in nature, its high energy content (120.7 kJ g^{-1}), and the fact that its combustion does not generate any environmental pollution [21]. Among the sources of liquid hydrogen, ethanol is a more sustainable option due to its renewable and biodegradable nature, low toxicity, and high availability. Thus, ethanol can be converted into a rich mixture of hydrogen through the catalytic steam reforming process (reaction 1) [21]:

$$C_2H_5OH + 3H_2O \rightarrow 2CO_2 + 6H_2. \quad (1)$$

There are several processes for hydrogen production, such as electrolysis, photolysis, and thermolysis of water, hydrolysis of hydrides, biological reactions, gasification and pyrolysis of biomass, steam reforming and dehydrogenation of alcohols, and partial oxidation of hydrocarbons [22–26]. The photocatalytic production of hydrogen from ethanol has gained prominence in recent years. However, the process is expensive due to the high electricity demand and electrode values [27]. The use of ethanol in the steam reforming process has advantages when compared to derivatives of fossil fuels, due to some of its features, as previously mentioned. Moreover, under steam reforming process conditions, its reaction with water is thermodynamically feasible generating a hydrogen-rich mixture. However, as a disadvantage, non-desired reactions can occur, such as decomposition and dehydration of ethanol, resulting in some products (CH_4 and C_2H_4) that can lead to coke formation causing the catalyst deactivation and consequently hindering hydrogen production [28]. In the ESR, noble metal catalysts (Au, Ru, Pt, Pd, and Rh) have high selectivity for the production of hydrogen [21], being, however, not economically viable [29]. Thus, non-noble metals, such as Cu, Ni, and Co are the most active metals for catalytic ESR [30].

2. Experimental

2.1. Synthesis of catalysts

$NiMoO_4$ catalysts were synthesized by the proteic sol-gel method. For this, 50% w/w of tasteless and colorless edible gelatin (Dr. Oetker) was weighed and dissolved in distilled water at 40 °C under constant stirring for sufficient time to ensure a homogeneous, dispersed mixture. Then, stoichiometric amounts of $(NH_4)_6Mo_7O_{24}.4H_2O$ (6.5 mmol) and $Ni(NO_3)_2.6H_2O$ (45.8 mmol) were added separately into the solution containing the gelatin. NaOH (1.3 mmol) was then added to the solution containing the mixture of gelatin and ammonium molybdate to favor the hydrolysis of the polyoxometalate anions to the orthomolybdate (MoO_4^{2-}) anions. Finally, the solution containing nickel nitrate and gelatin was poured into this solution dropwise, maintaining the same temperature and stirring conditions. The resulting mixture was taken to the oven and dried at 100 °C, obtaining the so-called "*puff*" precursor. The precursor was calcined in a furnace at temperatures ranging from 300 °C to 1000 °C. The obtained materials were then named according to their calcination temperatures.

2.2. Characterization techniques

X-ray diffraction (XRD) was used for the structural characterization of the synthesized materials using a PANalytical diffractometer, model X'Pert3 Powder. The measurements were collected in the range from 5 to 90 °2θ, using Cu Kα radiation (λ = 1.5406 Å). In order to calculate the lattice parameters, the MDI Jade 9.0 was employed. Morphological analyses of the $NiMoO_4$ catalysts were evaluated by using a TESCAN scanning electron microscope model VEGA3. X-ray microchemical analyses and elemental mapping of the samples were carried out using an Oxford Instruments X-act PentaFET microscope. For the transmission electron microscopy (TEM), energy dispersive spectroscopy (EDS), and electron energy-loss spectroscopy (EELS) measurements it was used a Tecnai G2-20 instrument (FEI).

The thermal behavior of the precursor and the edible gelatin was investigated using two thermal analyzers: (i) TGA Q50 TA Instruments, and (ii) 2960 SDT V3.0F TA Instruments. The samples were analyzed under a nitrogen gas flow of 20 mL min^{-1}, with heating at 20 °C min^{-1} from room temperature to 1000 °C. Raman spectra of the as-synthesized catalyst were acquired in backscattering configuration, using a Horiba/Jobin-Yvon LABRAM-HR spectrometer with an Olympus confocal microscope attached to the equipment. The 632.8 nm line of a He–Ne laser was used for excitation and an edge filter was employed for the rejection of stray light. UV–vis spectra were recorded at room temperature using a Shimadzu UV-2600 spectrophotometer equipped with an integrating sphere and operated in a diffuse reflection mode. The medium scan speed was applied in the range from 200 to 800 nm, and the $BaSO_4$ was used as reference material. The colorimetric parameters were determined according to the CIE L*a*b* method [31], using a Pantone® Color Cue®2 handheld color analysis device.

2.3. Catalytic tests

The catalytic tests were performed at atmospheric pressure in a fixed bed quartz tubular reactor with a 5 mm internal diameter at 400, 500, and 600 °C. Approximately 100 mg of sample was used which was inserted into a vertical furnace equipped with a thermocouple for temperature control. Before the catalytic reactions, the samples were thermally treated with nitrogen (flowing 30 mL min^{-1}) at 450 °C, for 1 h. The reactor was fed with a mixture of water/ethanol in the ratio 3:1. The flow rate of the nitrogen used as transport gas was adjusted to 20 mL min^{-1}. The reactants and products obtained after the reaction were analyzed in a gas chromatograph model Agilent 7890 A.

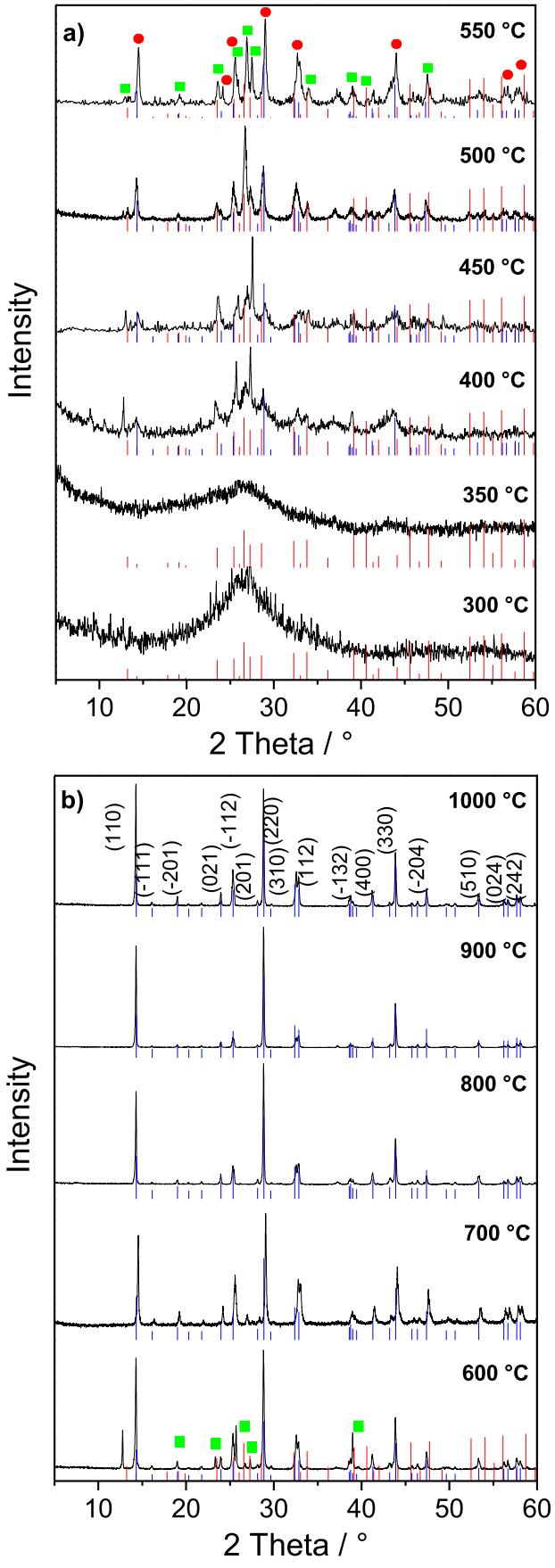

(caption on next column)

Fig. 1. XRD patterns for all $NiMoO_4$ catalysts synthesized. (a) Calcined samples from 300 °C to 550 °C, and (b) samples prepared in the temperature range 600–1000 °C. In red lines, the reference ICDD card #012–0348 (β), whose characteristic planes are indicated by green squares ( ). In blue lines, the reference card #031–0902 with the main crystallographic planes is indicated by red circles ( ). (For interpretation of the references to color in this figure legend, the reader is referred to the Web version of this article.)

3. Results and discussion

$NiMoO_4$ catalysts were synthesized by the proteic sol-gel method using edible gelatin. According to Rivero et al. [32], gelatin is a mixture of several amino acids that interact through peptide bonds with other amino acid chains through hydrogen bonds to give a structure called "*triple helix*". Thus, the triple helix structure in contact with identical structures acquires an unfolded form, which favors the interaction of the gelatin with the metallic ions during synthesis. Under heating, the α-helix of the gelatin with the coiled structure disintegrates forming the primary structures. Regions rich in proline and hydroxyproline proteins elicit the "*sol*" to "*gel*" the transition in the gelatin [32]. Then, the reactive groups of the gelatin, i.e. NH_3^+ and COO^- interacting with the molybdate (MoO_4^{2-}) and nickel (Ni^{2+}) ions, respectively, in order to form the "*puff*". The diversity of side chains present in the edible gelatin structure makes it an essential gelling agent for the proteic sol-gel reactions.

Before testing the catalytic applications in the steam reforming reactions of ethanol for hydrogen production, the materials were structurally and morphologically characterized. Fig. 1 shows the XRD data obtained for samples treated at different calcining temperatures from 300 °C to 1000 °C. It was not possible to obtain the diffractogram for the precursor (called "*puff*") because of its gel form, thus making it impossible to carry out the measurement. We can observe that the samples are amorphous at 300 °C and 350 °C with a tendency to form the β-$NiMoO_4$ polymorph, as indicated by ICDD (The International Centre for Diffraction Data) card #012–0348 (see red lines in Fig. 1a). It is important to emphasize that by this methodology the hydrated precursor ($NiMoO_4.xH_2O$) was not obtained, as previously reported when the hydrothermal process or coprecipitation was employed [16,33,34]. The samples calcined in the temperature range 400–600 °C exhibited mixtures of β- and α-$NiMoO_4$ phases. The α-phase is indicated by the ICDD card #031–0902 (see the blue lines in Fig. 1a). The characteristic planes of β- and α-phases (Miller indexes) were identified by green squares and red circles, respectively. Concerning the samples calcined in the range 700–1000 °C, all materials have crystallized as the α polymorph without impurities or secondary phases.

In Fig. 1b, the main crystallographic planes of the α-phase were indicated, according to the ICDD card #031–0902. Although the sample calcined at 600 °C crystallized preferentially as the α-phase, it is possible to observe some characteristic planes of the β-phase, as indicated by the green squares. Therefore, our results suggest that only phase-pure α polymorphs occurred below 700 °C, being the β-phase not produced in its crystalline form under the experimental conditions employed. As it is well known, all the $NiMoO_4$ polymorphs (α and β) exhibited monoclinic structures with space group *C*2/*m* (#12) with eight formula-units per unit cell. In the α-form, Ni^{2+} and Mo^{6+} ions occupy octahedral sites, while in the β-form, Ni^{2+} still in octahedral sites, and Mo^{6+} ions are in tetrahedral sites [17,20,34].

The lattice parameters were calculated only for phase-pure, homogeneous samples (600–1000 °C) by using the MDI Jade 9.0 software, and the values are presented in Table 1. The Jade 9.0 software allows the calculation of the lattice parameters from the experimental data (XRD) and the initial parameters provided by the standards used in indexing, in this case, ICDD card #031–0902. The calculated values are in good agreement with ICDD card and exhibited minor changes as the

Table 1
Lattice parameters and crystallite sizes for the $NiMoO_4$ catalysts obtained at different calcining temperatures. Reference data is shown for comparison.

Temperature (°C)	*a* (Å)	*b* (Å)	*c* (Å)	*β* (°)	*V* (Å^3)	Crystallite Size (nm)
600	9.59	8.75	7.66	114.19	578.21	33
700	9.59	8.75	7.66	114.24	587.04	49
800	9.59	8.75	7.66	114.25	586.87	51
900	9.59	8.75	7.66	114.23	586.85	58
1000	9.58	8.75	7.66	114.14	587.08	61
ICDD #031-0902	9.59	8.75	7.65	114.24	586.20	–

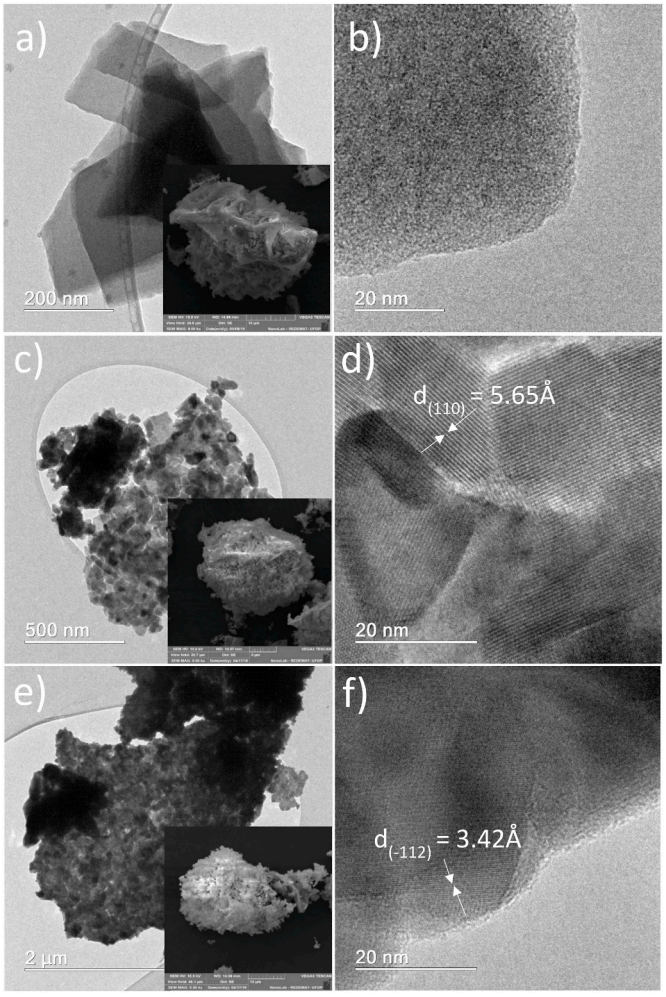

Fig. 2. TEM images showing the nanosized particles and SEM images (insets) for catalysts calcined at (a) 300 °C, (c) 500 °C, and (e) 700 °C. HRTEM images in high magnification for samples obtained at (b) 300 °C, (d) 500 °C, and (f) 700 °C.

temperature increased. The average crystallite sizes of the catalysts were calculated using the Debye-Scherrer formula:

$$L = \frac{0.90\lambda}{\beta \cos\theta}, \quad (1)$$

For this calculation, it was used the average of the two most intense planes. The crystallite sizes grew from 33 to 61 nm, as the calcining temperature increased, as expected.

In order to investigate the morphological characteristics of the catalysts obtained by the proteic sol-gel method, electron microscopy measurements (SEM and HRTEM) were performed. Fig. 2 shows the

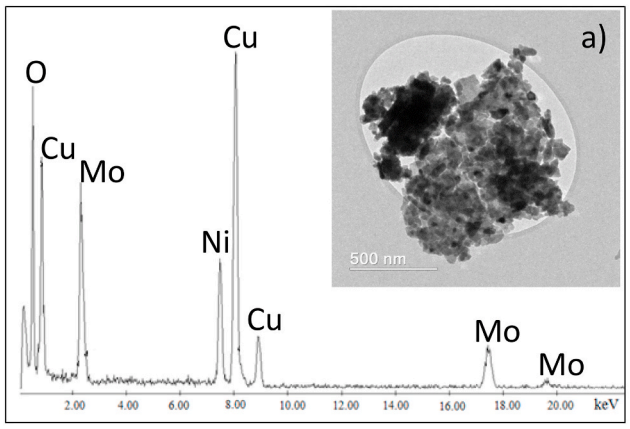

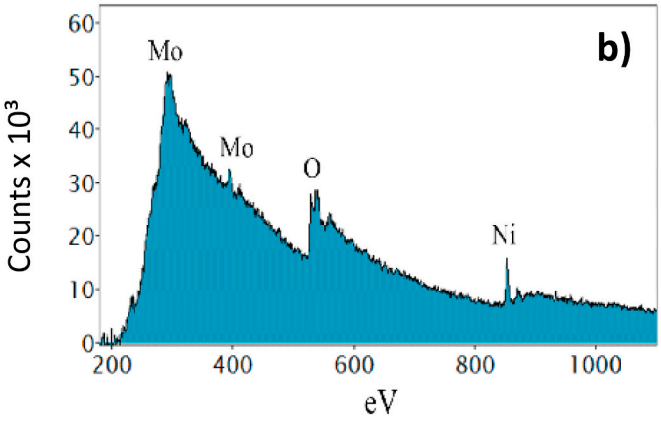

Fig. 3. (a) EDS spectrum of the sample calcined at 500 °C showing the chemical composition of the sample. Inset: region of the sample selected for the chemical analysis. (b) EELS spectrum evidencing the characteristic bands of the chemical elements molybdenum, oxygen, and nickel.

results for the samples calcined at 300, 500, and 700 °C. Fig. 2a, c, and 2e show representative TEM images, in which nanosized particles can be visualized for samples treated at 300, 500, and 700 °C, respectively. The insets exhibit typical SEM images of the same samples. As can be seen, similar morphologies were obtained; however, the agglomerates exhibited different sizes. It was observed that the sample produced at 300 °C presented smaller agglomerates resulting in smaller particle sizes. Fig. 2b, d, and 2f present the HRTEM images of the samples calcined at 300, 500, and 700 °C, respectively. It was not possible to observe the crystallographic planes for the sample obtained at 300 °C. However, the presence of two-dimensional lattice fringes illustrates that the particles in the range of 500–700 °C are polycrystalline. Interplanar spacings were computed to be about 0.56 nm for the sample prepared at 500 °C, which corresponds to the (110) planes, and about 0.34 nm for the sample prepared at 700 °C, corresponding to the (−112) planes.

The chemical purity of the as-synthesized catalysts was investigated by EDS and EELS measurements. Considering that all materials were prepared starting from the same precursor (*"puff"*), a typical sample (500 °C) was chosen for this investigation, and the results were extended to the other catalysts calcined at different temperatures. Fig. 3a shows the EDS spectrum obtained for samples at 500 °C and the selected region is displayed as an inset. We can observe the presence of the oxygen (O), molybdenum (Mo), and nickel (Ni) ions, as expected. It is important to emphasize that the presence of the peaks referring to the copper (Cu) element can be attributed to the grids used during the preparation of the

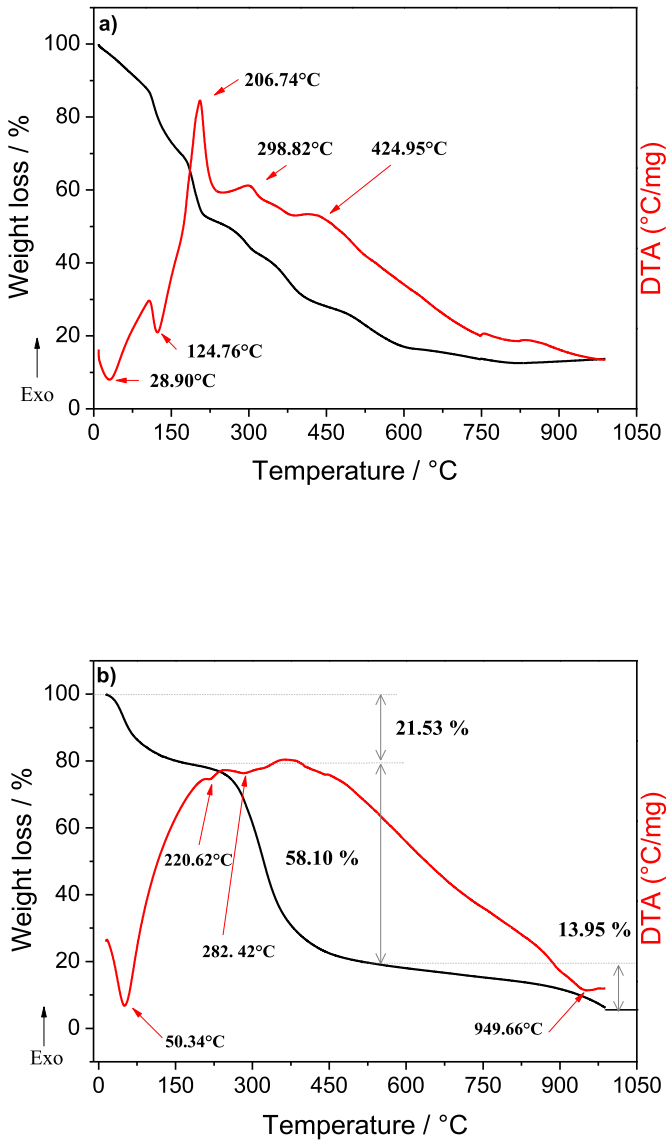

Fig. 4. TG (black) and DTA (red) curves under nitrogen atmosphere for (a) the precursor (*"puff"*), and (b) the edible gelatin used in the synthesis. (For interpretation of the references to color in this figure legend, the reader is referred to the Web version of this article.)

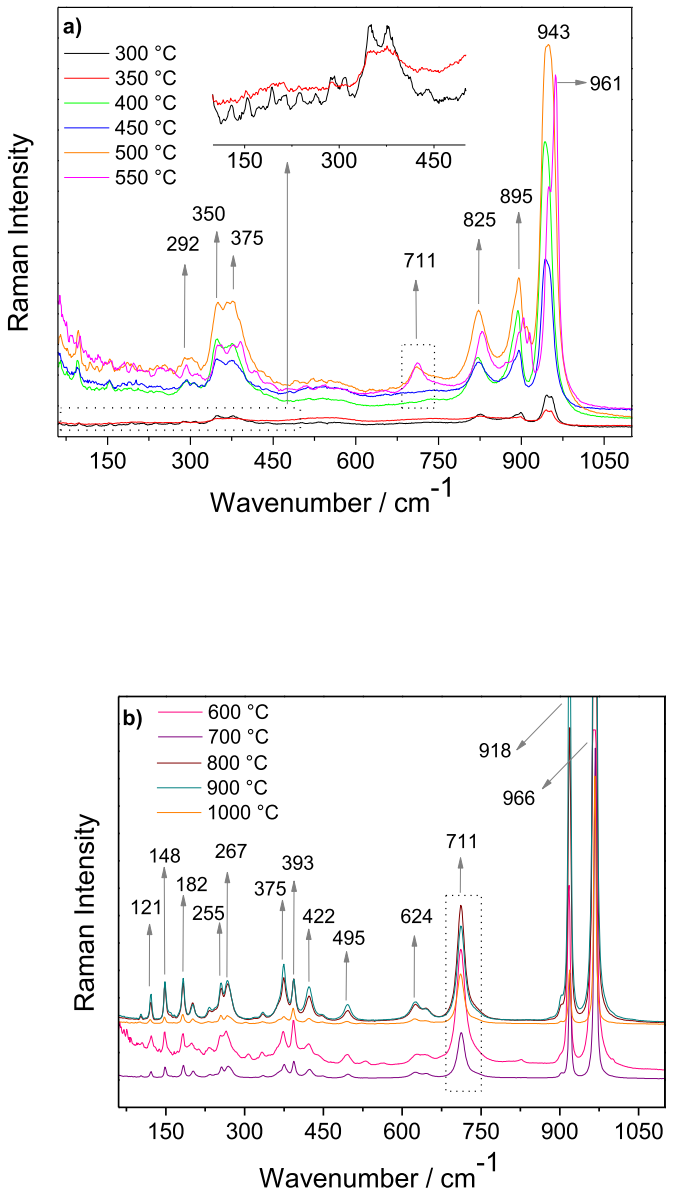

Fig. 5. Micro-Raman spectra for the catalysts treated at different temperatures: (a) 300–550 °C; (b) 600–1000 °C. The inset in (a) shows the amplification of the wavenumber region 100-500 cm^{-1} to facilitate the observation of these low-intensity modes.

samples. Furthermore, Fig. 3b shows the electron energy-loss spectrum of the sample calcined at 500 °C, in order to complement the chemical analysis of these catalysts. It is known that this technique allows detecting elements present even in small concentrations [35]. In the EELS spectrum, the characteristic energies of molybdenum ($M_{4,5}$ = 227 eV and M_3 = 392 eV), nickel (L_3 = 855 eV), and oxygen (K = 532 eV) were clearly identified [36]. Thus, from both techniques (EDS and EELS) it was possible to attest to the chemical purity of the samples.

The thermal stability of the precursor sample (*"puff"*) and the edible gelatin were investigated through thermogravimetric (TG) and differential thermal analysis (DTA). Fig. 4 presents the thermogravimetric curves for these samples under heating, showing their weight loss as a function of temperature. This behavior is represented by the TG curves (in black) and DTA curves (in red). Thus, in Fig. 4a we can observe the results of precursor (*"puff"*), where the greatest mass loss occurred in the range of 25 °C–300 °C. In this temperature range, about 60% of the initial amount was lost. It is believed that this lost portion is mainly due to water evaporation, nitrate decomposition, and molybdate that did not react. As well as the beginning of sample crystallization and fusion of organic matter present in gelatin, i.e., amino acids and proteins. Other mass loss characterized by an irreversible process occurred around 424 °C and it is suggested the structural conversion of the precursor sample into the compound formed by the mixture of β+α phases. Finally, a lower mass loss is observed above 500 °C. This loss is associated with the loss of remaining organic matter, such as CO_2 and CO gases as it can be best elucidated from the results obtained for pure gelatin. It is noteworthy that the synthesis via proteic sol-gel methodology finishes after calcination at temperatures high enough to evaporate the organic matter [1–7].

In order to elucidate the weight losses, which are characteristic of the edible gelatin used in the synthesis of the catalysts, the TG/DTA curves for the gelatin are presented in Fig. 4b. We can observe endothermic peaks centered at 50.34 °C, 220.62 °C, 282.42 °C, and 949.66 °C. We can divide the weight losses in the gelatin into three different regions: (i) the first weight loss corresponds to 21.5% of the initial mass and occurs up to approximately 200 °C, which are related to the evaporation of

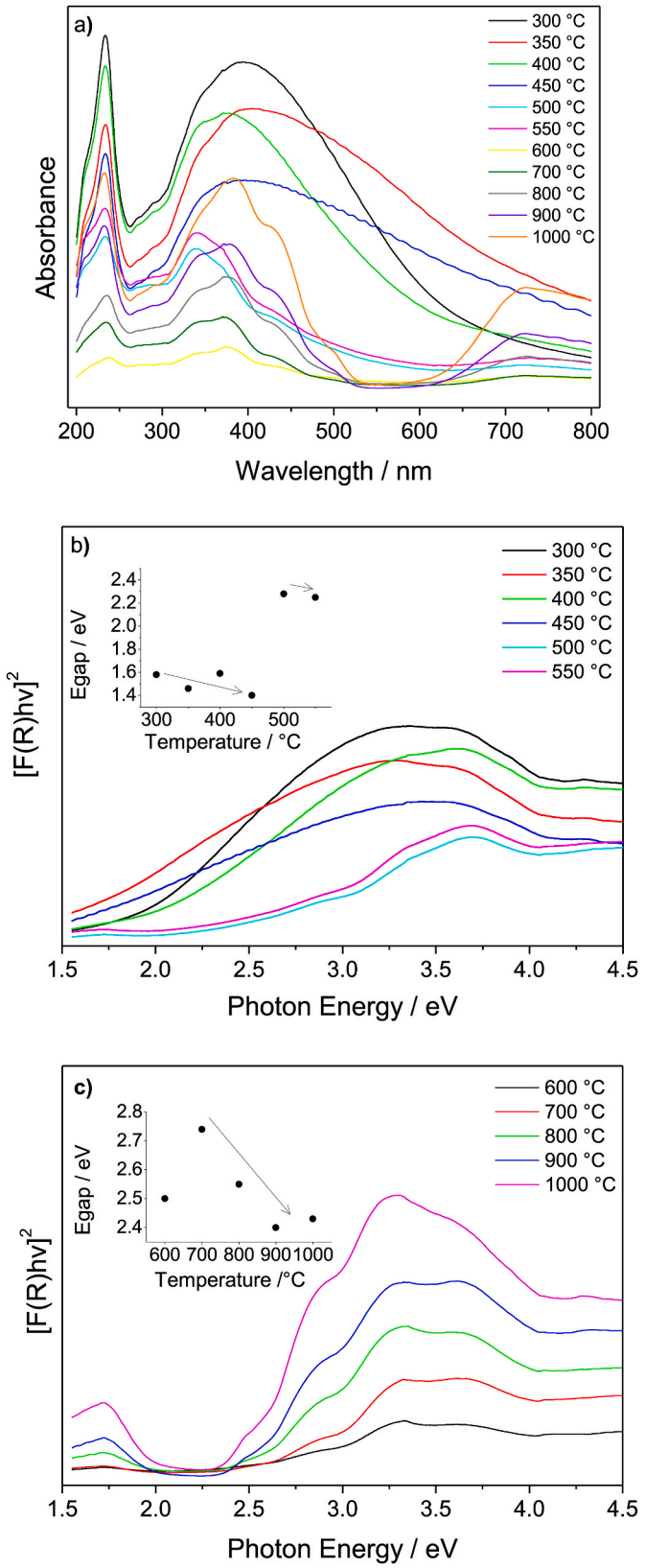

Fig. 6. (a) Absorbance versus wavelength plot for the as-synthesized catalysts. (b) Kubelka-Munk function against the photon energy for the samples calcined in the temperature range 300–550 °C; and (c) 600–1000 °C. The insets show the relations between gap energy and temperature.

physical water by evaporation process; (ii) the second weight loss occurs in the range 200–550 °C (corresponds to a 58% of the initial amount) and is related to the fusion of organic matter (amino acids and proteins); (iii) finally, the last (and the lowest) weight loss is observed above 550 °C (14% of the initial mass) and is associated with the remaining organic matter.

Micro-Raman spectroscopy data were collected in order to investigate the catalysts based on their optical-vibration properties as a function of the chemical elements present in its structure. Fig. 5a exhibits the spectra obtained from the calcined samples in the range 300–550 °C, while the samples treated at higher temperatures (600–1000 °C) are shown in Fig. 5b. The results indicate that all samples exhibit short-range structural ordering, even samples calcined at lower temperatures (300 and 350 °C). The spectra showed a very strong band at around 950 cm^{-1}, strong bands at 918 and 711 cm^{-1}, and many bands in the range 60–600 cm^{-1}. These results are in agreement with previous studies [37–41].

The absorbance spectra for all the catalysts obtained through the proteic sol-gel methodology is shown in Fig. 6. The spectra patterns are a consequence of the absorption band *d-d* from Ni^{2+}, and the band of charge transfer $O^{2-} \rightarrow Mo^{6+}$ [18]. We can observe a high percentage of absorption throughout the visible region due to a high degree of lightness in the molybdates. Furthermore, the catalysts exhibited different colors, according to the heat treatment and the crystal structure [34].

The Kubelka-Munk transformations for samples are presented in Fig. 6b and c. The optical bandgap energies (E_g) were estimated using the method proposed by Wood and Tauc [42]. The gap values obtained for direct allowed transitions ranged from 1.46 to 2.74 eV, which are in agreement with the literature [34,38,43,44] and are presented in the inset of Fig. 6b and c as a function of temperature. The E_g values tended to decrease for increasing temperatures, because the α-phase has the lowest E_g value among the other polymorphs [20] and, in our case, the α-phases were produced at higher temperatures (>600 °C). The calcining temperature increase in $NiMoO_4$ enabled increased coordination of oxygen around the metal, hence influencing the bandgap energy. The charge transfer energy, decreased with the greater ordering of the crystal structure, in agreement with the XRD results (see Fig. 1). According to the literature, the values found for the gap energy make the samples potential catalysts [45]. These results led us to apply our materials in the ethanol steam reforming for hydrogen production, as will be discussed later. The optical bandgap values and colorimetric parameters (L*, a*, b*, C_{ab}, h°) are shown in Supporting Information, as well as, the photograph of the catalysts illustrating the actual color of the powders (see Table S1) [46,47].

After synthesis and characterization, the $NiMoO_4$ materials calcined at 300, 500 and 700 °C were then evaluated as catalysts towards the ethanol steam reforming aiming the hydrogen production. These three samples were chosen based on the literature reports indicating that the β-phase performs better in catalysis when compared to the α-phase [48]. Although phase-pure β-$NiMoO_4$ materials were not obtained by the sol-gel methodology using edible gelatin, our results indicated that in low-temperature calcined samples, the amorphous *"puff"* tended to form the β-phase, which justifies the choice for the calcined samples at 300 and 500 °C. Besides, a phase pure α-$NiMoO_4$ sample was chosen for comparison purposes. Thus, the sample calcined at 700 °C was chosen because it presented the smallest particle size amongst the samples that crystallized in the α-phase (see Table 1). Herein, a series of experiments studying the ethanol conversion and product distribution as a function of the reaction temperature were performed to compare the samples, and the results are presented in Fig. 7 to ESR reactions at 400 °C (Figs. 7a), 500 °C (Figs. 7b) and 600 °C (Fig. 7c). Fig. 7 emphasizes the percentage selectivity of main products, i.e., hydrogen, methane, carbon monoxide, and carbon dioxide, as well as the ethanol conversion. Table S2 in the Supporting Information shows all results, including other secondary products as ethylene, acetone, and acetaldehyde at 8 h, 16 h, and 24 h reaction times.

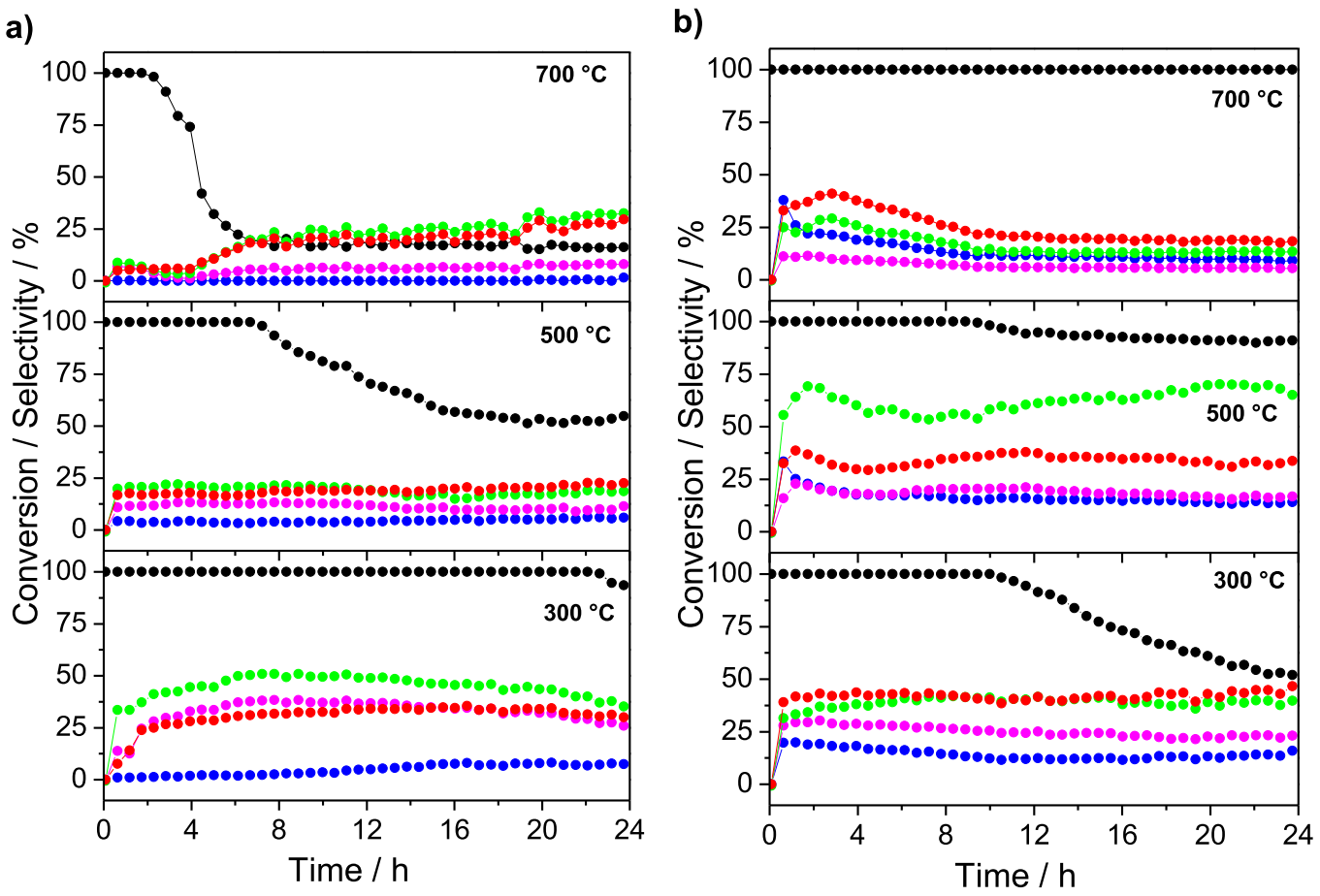

Fig. 7. Conversion/selectivity plots (%) due to time (h) showing the efficiency of $NiMoO_4$ calcined at 300 °C, 500 °C and 700 °C as catalysts for ESR. Products detected are presented by circles: CH_3CH_2OH (black), H_2 (red), CO (green), CH_4 (magenta) and CO_2 (blue), (a) Reaction temperature of 400 °C; (b) Reaction temperature of 500 °C; (c) Reaction temperature of 600 °C. (For interpretation of the references to color in this figure legend, the reader is referred to the Web version of this article.)

Interestingly, all obtained catalysts were active in the process, achieving the complete conversion of ethanol under all tested temperatures. However, some differences in the product distribution were detected when the reaction temperature and the type of catalyst varied. The main products detected were hydrogen, methane, acetaldehyde, and carbon oxides (CO and CO_2). In some cases, there were low quantities of ethylene. The amount of acetaldehyde present indicates that the main route of ethanol steam reforming goes through its dehydrogenation (reaction 2). However, the presence of ethylene in a small amount, detected in some tests, points to some contribution of ethanol dehydration (reaction 3), as verified by Arapova et al. [49]:

$$C_2H_5OH \rightarrow CH_3CHO + H_2, \quad (2)$$

$$C_2H_5OH \rightarrow C_2H_4 + H_2O. \quad (3)$$

Fig. 7a shows the results for the reactions conducted at 400 °C. We can observe that in this condition the catalyst calcined at 300 °C, presented H_2, CO, and CH_4 as major products indicating that the acetaldehyde is decomposed into CO and CH_4 (reaction 4). The highest selectivity to CO and the small amount of CO_2 indicate that the reverse water-gas shift reaction (reaction 5) would be taking place:

$$CH_3CHO \rightarrow CH_4 + CO, \quad (4)$$

$$CO_2 + H_2 \rightarrow CO + H_2O. \quad (5)$$

For the reaction at 400 °C, the conversion of ethanol reached 100% in the tests with catalysts calcined at 300 °C. However, the ethanol conversion dropped to 60% and 20%, when were used the catalysts calcined at 500 °C and 700 °C, respectively. This dropping was accompanied by a significant increase in acetaldehyde formation as well as a decrease in the selectivity toward CH_4. This indicates that at this stage the ethanol dehydrogenation (reaction 2) is favored. The decrease in CH_4 selectivity may be due to the methane steam reforming (reaction 6) and decomposition reactions (reaction 7) [50]:

$$CH_4 + H_2O \rightarrow CO + 3H_2, \quad (6)$$

$$CH_4 \rightarrow 2H_2 + C. \quad (7)$$

Similar behavior was exhibited by catalysts when the reaction was conducted at 500 °C and the results are presented in Fig. 7b. We can observe an increase in acetaldehyde formation, with time on stream, and a deactivation only when calcined catalysts at 300 and 500 °C were used. Thus, high performance was maintained by catalysts at 700 °C without catalytic deactivation. It is interesting to note that the reaction temperature increasing to 500 °C also produced an increase in H_2 and CO_2 selectivities, indicating that the ethanol steam reforming (reaction 1) is involved. Finally, the results for ERS with reaction temperature at 600 °C are presented in Fig. 7c. Over the entire period of 24 h of reaction, the complete conversion of ethanol was achieved with practically no catalytic activity loss, for all catalysts used. Selectivity toward H_2 was still higher and reached a maximum, close to 60%, for catalyst calcined at 700 °C.

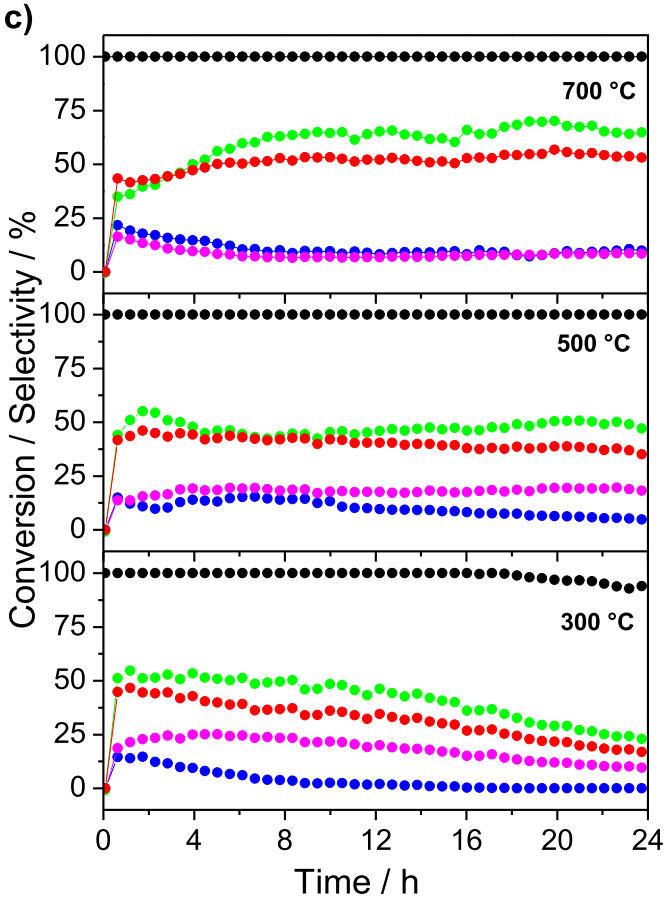

Fig. 7. (*continued*).

It was observed that ethanol conversion decreased with time on stream in some experiments. The analysis of spent catalysts revealed carbon materials deposited. Commonly, as observed in deactivated catalysts, two types of carbonaceous deposits, which depend on the operational conditions, have been reported, amorphous carbon and filamentous carbon, leading to different levels of deactivation [51]. From the part of the experiments where the catalyst deactivation occurred, it was observed an increase in acetaldehyde formation most probably due to carbon deposition on its surface. Thus, we can speculate that coke mainly comes from CH_3CHO (reaction 8):

$$CH_3CHO \rightarrow \text{coke}. \quad (8)$$

However, the decomposition of methane (reaction 7), which can also contribute to carbon deposition, cannot be ruled out [50]. In this case, coke formation can be verified by Raman spectroscopy. Fig. 8 presents the Raman spectra for the catalysts spent in experimental assays at 500 °C (reaction temperature). In Fig. 8a, it is possible to observe that even after the test the catalyst presents the vibrational modes characteristic of nickel molybdate and, in this case, the deactivation of the catalyst was not observed, as shown in Fig. 7b when was used the catalysts calcined at 700 °C. On the other hand, Fig. 8b shows two bands centered at 1337 cm^{-1} and 1590 cm^{-1}, which are characteristic of graphite materials (*D* and *G* bands, respectively) [52]. In this case, it is observed that the bands *D* and *G* are very intense and hidden the presence of the vibrational modes of $NiMoO_4$, suggesting the presence of deposited coke in a big amount. This result corroborates the data discussed in Fig. 7b (for catalyst calcined at 300 °C), where the catalyst deactivation was observed.

4. Conclusions

In this work, catalysts based on nickel molybdates were synthesized via the proteic sol-gel process and were used in the production of hydrogen from ethanol steam reforming. The proteic sol-gel synthesis is within the current context of so-called *"Green Chemistry"* and stands out for not generating toxic residues and due to its low cost. The catalysts were thoroughly characterized and the results indicated that different products were produced according to the calcination temperature. At lower temperatures, a mixture of α and β polymorphs was produced and only above 700 °C the homogeneous α product was obtained. The methodology did not allow the production of β polymorph and neither the hydrated phase of nickel molybdate. The α phase crystallized in the monoclinic arrangement C2/m (#12) and presented distinct colors. A colorimetric study was carried out on the samples using the CIE L*a*b* system to qualify the colors resulting from the powders. The powder colors ranged from brown shades to yellowish-green as the temperature increased. The gap energy of the materials was determined using the method proposed by Wood and Tauc and values range from 1.40 to 2.74 eV.

For catalysis tests, were used the samples calcined at 300 °C, 500 °C and 700 °C and three distinct reaction temperatures were investigated, i.e., 400 °C, 500 °C and 600 °C. The results showed that the reaction temperature influences quantitatively on the formed products. In general, the catalysts exhibited good performance, but the samples calcined at 700 °C exhibited the best catalytic activity that could be expressed according to the selectivity content of the hydrogen. Besides, in some cases, the catalyst deactivation was observed, which was justified by the presence of coke deposited on the sample surface, and was evaluated by Raman vibrational spectroscopy. This technique proved the presence of bands D and G, characteristics of graphite materials, supporting our

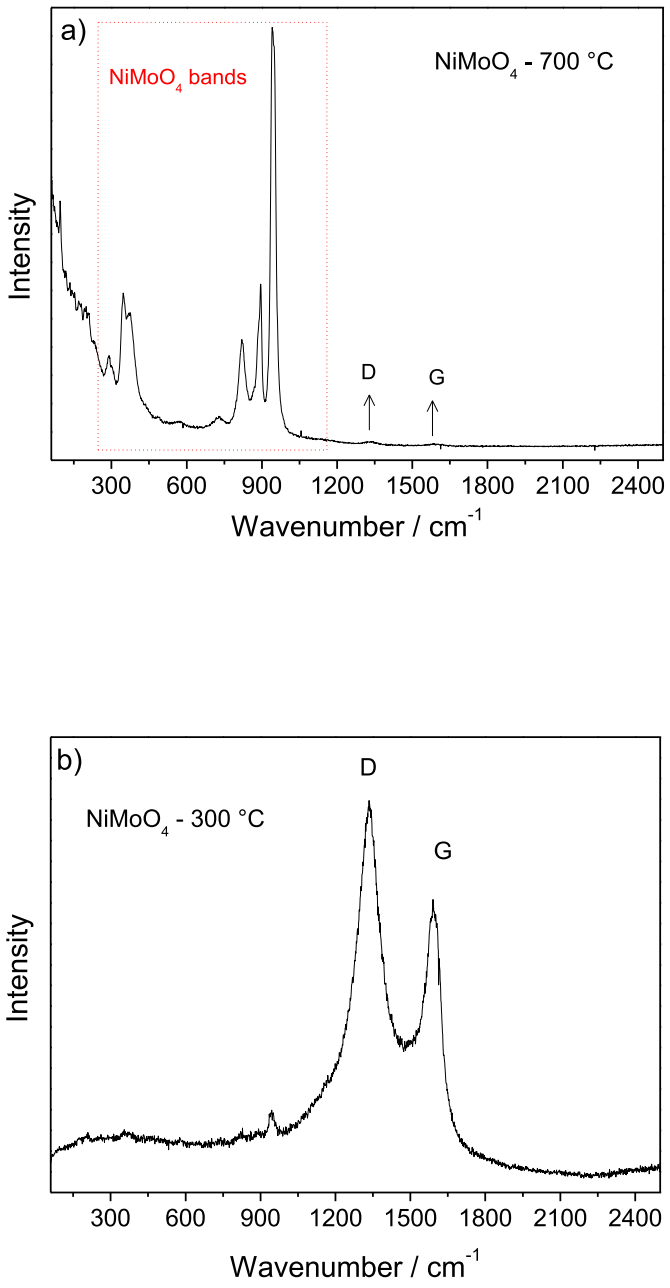

Fig. 8. Raman spectra for the $NiMoO_4$ catalysts spent after the ESR from the reaction temperature of 500 °C. (a) Catalyst calcined at 700 °C; (b) catalyst calcined at 300 °C

proposal. Thus, the work reports the unprecedented use of nickel molybdates for hydrogen production via ethanol steam reforming and the use of edible gelatin in the production of catalysts, bringing important contributions to sustainability in the field of chemistry.

CRediT authorship contribution statement

Maíra V. da Silva: Investigation, Methodology, Data curation, Writing - original draft. **Humberto V. Fajardo:** Validation, Investigation. **Thenner S. Rodrigues:** Methodology, Data curation, Validation. **Felipe A. e Silva:** Methodology, Data curation. **Vanderlei S. Bergamaschi:** Methodology, Data curation, Validation. **Anderson Dias:** Investigation, Validation. **Kisla P.F. Siqueira:** Conceptualization, Writing - review & editing, Supervision, Funding acquisition.

Declaration of competing interest

The authors declare that they have no known competing financial interests or personal relationships that could have appeared to influence the work reported in this paper.

Acknowledgments

This work was supported by FAPEMIG, CNPq, and UFOP. Special tanks are due to Dra. Rosa Malena Fernandes Lima for XRD measurements. The Center of Microscopy at the Universidade Federal de Minas Gerais (http://www.microscopia.ufmg.br) is also acknowledged for providing the equipment and technical support for experiments involving electron microscopy.

Appendix A. Supplementary data

Supplementary data to this article can be found online at https://doi.org/10.1016/j.matchemphys.2021.124301.

References

[1] J.A.C. Paiva, M.P.F. Graça, J. Monteiro, M.A. Macedo, M.A. Valente, Spectroscopy studies of $NiFe_2O_4$ nanosized powders obtained using coconut water, J. Alloys Compd. 485 (2009) 637–641.
[2] W.M.S. Silva, N.S. Ferreira, J.M. Soares, R.B. Silva, M.A. Macêdo, Investigation of structural and magnetic properties of nanocrystalline Mn-doped $SrFe_{12}O_{19}$ prepared by proteic sol-gel process, J. Magn. Magn Mater. 395 (2015) 263–270.
[3] M.A.P. Buzinaro, N.S. Ferreira, F. Cunha, M.A. Macêdo, Hopkinson effect, structural and magnetic properties of M-type Sm^{3+}-doped $SrFe_{12}O_{19}$ nanoparticles produced by a proteic sol-gel process, Ceram. Int. 42 (2016) 5865–5872.
[4] P.M. Pimentel, S.V.M. Lima, A.F. Costa, M.S.C. Câmara, J.D.C. Carregosa, R.M.P. B. Oliveira, Gelatin synthesis and color properties of (La, Pr, Nd) lanthanide aluminates, Ceram. Int. 43 (2017) 6592–6596.
[5] M.S. Pereira, T.S. Riberio, F.A.S. Lima, L.P.M. Santos, C.B. Silva, P.T.C. Freire, I. F. Vasconcelos, Synthesis and properties of $Sn_{1-x}Fe_xO_2$ nanoparticles obtained by a proteic sol-gel method, J. Nanoparticle Res. 20 (2018) 212.
[6] M.A. Macedo, J.M. Sasaki, Brazilian Patent PI 0203876-5/BR, 2002.
[7] F.S. Oliveira, P.M. Pimentel, R.M.P.B. Oliveira, D.M.A. Melo, M.A.F. Melo, Effect of lanthanum replacement by strontium in lanthanum nickelate Crystal synthesized using gelatin as organic precursor, Mater. Lett. 64 (2010) 2700–2703.
[8] N.A.S. Nogueira, V.H.S. Utuni, Y.C. Silva, P.K. Kiyohara, I.F. Vasconcelos, M.A. R. Miranda, J.M. Sasaki, X-ray diffraction and Mossbauer studies on superparamagnetic nickel ferrite ($NiFe_2O_4$) obtained by the proteic sol-gel method, Mater. Chem. Phys. 163 (2015) 402–406.
[9] A.F. Costa, P.M. Pimentel, F.M. Aquino, D.M.A. Melo, I.M.G. Santos, Gelatin synthesis of $CuFe_2O_4$ and $CuFeCrO_4$ ceramic pigments, Mater. Lett. 112 (2013) 58–61.
[10] A.E. Danks, S.R. Hall, Z. Schnepp, The evolution of "sol-gel" chemistry as a technique for materials synthesis, Mater. Horiz. 3 (2016) 91–112.
[11] D. Cai, D. Wang, B. Liu, Y. Wang, Y. Liu, L. Wang, H. Li, H. Huang, Q. Li, T. Wang, Comparison of the electrochemical performance of $NiMoO_4$ nanorods and hierarchical nanospheres for supercapacitor applications, Appl. Mater. Interfaces 5 (2013) 12905–12910.
[12] Y. Sun, X. Hu, W. Luo, J. Shu, Y. Huang, Self-assembly of hybrid Fe2Mo3O8-reduced graphene oxide nanosheets with enhanced lithium storage properties, J. Mater. Chem. A. 1 (2013) 4468–4474.
[13] Y. Li, H. Wang, J. Jian, Y. Fan, L. Yu, G. Cheng, J. Zhou, M. Sun, Design of three dimensional hybrid Co_3O_4@$NiMoO_4$ core/shell arrays grown on carbon cloth as high-performance supercapacitors, RSC Adv. 6 (2016) 13957–13963.
[14] W. Xiao, J.S. Chen, C.M. Li, R. Xu, X.W. Lou, Synthesis, characterization, and lithium storage capability of $AMoO_4$ (A = Ni, Co) nanorods, Chem. Mater. 22 (2010) 746–754.
[15] J. Liu, X. Huang, Y. Li, Z.A. Li, A general route to thickness-tunable multilayered sheets of scheelite-type metal molybdate and their self-assembled films, J. Mater. Chem. 17 (2007) 2754–2759.
[16] V. Jeseentharani, A. Dayalan, K.S. Nagaraja, Nanocrystalline composites of transition metal molybdate ($Ni_{1-x}Co_xMoO_4$; x = 0, 0.3, 0.5, 0.7, 1) synthesized by a co-precipitation method as humidity sensors and their photoluminescence properties, J. Phys. Chem. Solid. 115 (2018) 75–83.
[17] A.W. Sleight, B.L. Chamberland, Transition metal molybdates of the type $AMoO_4$, Inorg. Chem. 7 (1968) 1672–1675.
[18] V. Blanco-Gutierrez, A. Demourgues, M. Gaudon, Sub-micrometric β-$CoMoO_4$ rods: optical and piezochromic properties, Dalton Trans. 42 (2013) 13622–13627.
[19] V. Blanco-Gutierrez, L. Cornu, A. Demourgues, M. Gaudon, $CoMoO_4$/$CuMo_{0.9}W_{0.1}O_4$ mixture as an efficient piezochromic sensor to detect temperature/pressure shock parameters, ACS Appl. Mater. Interfaces 7 (2015) 7112–7117.

[20] L.C. Robertson, M. Gaudon, S. Jobic, P. Deniard, A. Demourgues, Investigation of the first-order phase transition in the $Co_{1-x}Mg_xMoO_4$ solid solution and discussion of the associated thermochromic behavior, Inorg. Chem. 50 (2011) 2878–2884.
[21] Y.C. Sharma, A. Kumar, R. Prasad, S.N. Upadhyay, Ethanol steam reforming for hydrogen production: latest and effective catalyst modification strategies to minimize carbonaceous deactivation, Renew. Sustain. Energy Rev. 74 (2017) 89–103.
[22] M. Balat, H. Balat, C. Öz, Progress in bioethanol processing, Prog. Energy Combust. Sci. 34 (2008) 551–573.
[23] I. Dincer, C. Acar, Review and evaluation of hydrogen production methods for better sustainability, Int. J. Hydrogen Energy 40 (2015) 11094–11111.
[24] H.N. Abdelhamid, M.N. Goda, A.E.A.A. Said, Selective dehydrogenation of isopropanol on carbonized metal–organic frameworks, Nano-Struct. Nano-Objects 24 (2020) 100605.
[25] A.A. Kassem, H.N. Abdelhamid, D.M. Fouad, S.A. Ibrahim, Hydrogenation reduction of dyes using metal-organic framework-derived CuO@C, Microporous Mesoporous Mater. 305 (2020) 110340.
[26] H.N. Abdelhamid, A review on hydrogen generation from the hydrolysis of sodium borohydride, Int. J. Hydrogen Energy 46 (2021) 726–765.
[27] M. Murdoch, G.I. Waterhouse, M.A. Nadeem, J.B. Metson, M.A. Keane, R.F. Howe, J. Liorca, H. Idriss, The effect of gold loading and particle size on photocatalytic hydrogen production from ethanol over Au/TiO_2 nanoparticles, Nat. Chem. 3 (2011) 489–492.
[28] L. Guerrero, S. Castillla, M. Cobo, Advances in ethanol reforming for the production of hydrogen, Quim. Nova 37 (2014) 850–856.
[29] H. Song, U.S. Ozkan, Changing the oxygen mobility in Co/Ceria catalysts by Ca incorporation: implications for ethanol steam reforming, J. Phys. Chem. 114 (2010) 3796–3801.
[30] S. Duan, S. Senkan, Catalytic conversion of ethanol to hydrogen using combinatorial methods, Ind. Eng. Chem. Res. 44 (2005) 6381–6386.
[31] Cie Comission International de l'Eclairage, Recommendations on Uniform Color Spaces, Color Difference Equations, Psychometrics Terms. Supplement N° 2 of CIE Pub. N° 15 (E1-1.31) 1971, Bureau Central de la CIE, Paris, 1978.
[32] S. Rivero, M. García, A. Pinotti, Correlations between structural, barrier, thermal and mechanical properties of plasticized gelatin films, Innovat. Food Sci. Emerg. Technol. 11 (2010) 369–375.
[33] Y. Ding, Y. Wan, Y.L. Min, W. Zhang, S.H. Yu, General synthesis and phase control of metal molybdate hydrates $MMoO_4.nH_2O$ (M = Co, Ni, Mn, n = 0, ¾, 1) nano/microcrystals by a hydrothermal approach: magnetic, photocatalytic, and electrochemical properties, Inorg. Chem. 47 (2008) 7813–7823.
[34] M.V. Da Silva, D.F.M. De Oliveira, H.S. Oliveira, K.P.F. Siqueira, Influence of temperature on the structural and color properties of nickel molybdates, Mater. Res. Bull. 122 (2020) 110665.
[35] M.A. Teixeira, A.B. Mageste, A. Dias, L.S. Virtuoso, K.P.F. Siqueira, Layered double hydroxides for remediation of industrial wastewater containing manganese and fluoride, J. Clean. Prod. 171 (2018) 275–284.
[36] http://www.eels.info/atlas.
[37] S.S. Saleem, Infrared and Raman spectroscopic studies of the polymorphic forms of nickel, cobalt and ferric molybdates, Infrared Phys. 27 (1987) 309–315.
[38] A.P. Moura, L.H. Oliveira, I.L.V. Rosa, C.S. Xavier, P.N.L. Filho, M.S. Li, F.A. L. Porta, J.A. Varela, Structural, optical, and magnetic properties of $NiMO_4$ nanorods prepared by microwave sintering, Sci. World J. 315084 (2015) 1–8.
[39] H.M. Abdel-Dayem, Dynamic phenomena during reduction of α-$NiMoO_4$ in different atmospheres: in-situ thermo-Raman spectroscopy study, Ind. Eng. Chem. Res. 46 (2007) 2466–2474.
[40] X. Zhao, J. Meng, Z. Yan, F. Cheng, J. Chen, Nanostructured $NiMoO_4$ as active electrocatalyst oxygen evolution, Chin. Chem. Lett. 30 (2019) 319–323.
[41] F. Nti, D.A. Anang, J.I. Han, Facilely synthesized $NiMoO_4/CoMoO_4$ nanorods as electrode material for high performance supercapacitor, J. Alloys Compd. 742 (2018) 342–350.
[42] D.L. Wood, J. Tauc, Weak absorption tails in amorphous semiconductors, Phys. Rev. B 5 (1972) 3144–3151.
[43] H.-Y. He, P. Chen, L.-Y. Cao, J. Lu, Surface alkaline-acidic and photocatalytic properties of $MMoO_4$ (M = Fe^{2+}, Co^{2+}, Ni^{2+}) nanoparticles in different media conditions, Res. Chem. Intermed. 40 (2014) 1525–1536.
[44] V. Umapathy, P. Neeraja, A. Manikandan, P. Ramu, Synthesis of $NiMoO_4$ nanoparticles by sol-gel method and their structural, morphological, optical, magnetic and photocatalytic properties, Trans. Nonferrous Metals Soc. China 27 (2017) 1785–1793.
[45] G. Kianpour, F. Soofivand, M. Badiei, M. Salavati-Niasari, M. Hamadanian, Facile synthesis and characterization of nickel molybdate nanorods as an effective photocatalyst by co-precipitation method, J. Mater. Sci. Mater. Electron. 27 (2016) 10244–10251.
[46] K. McLaren, The development of the CIE 1976 (L*a*b*) uniform colour space and colour-difference formula, J. Soc. Dye. Colour. 92 (1976) 338–341.
[47] A.K.V. Raj, P.P. Rao, T.S. Sreena, T.R.A. Thara, Pigmentary colors from yellow to red in $Bi_2Ce_2O_7$ by rare earth ion substitutions as possible high NIR reflecting pigments, Dyes Pigments 160 (2019) 177–187.
[48] B. Senthilkumar, D. Meyrick, Y.-S. Lee, R.K. Selvan, Synthesis and improved electrochemical performances of nano β-$NiMoO_4$-$CoMoO_4.H_2O$ composites for asymmetric supercapacitors, RSC Adv. 3 (2013) 16542–16548.
[49] M.V. Arapova, S.N. Pavlova, V.A. Rogov, T.A. Krieger, A.V. Ishchenko, A.-C. Roger, Ni(Co)-containing catalysts based on perovskite-like ferrites for steam reforming of ethanol, Catal. Sustain. Energy. 2 (2014) 10–20.
[50] A.S.P. Lovón, J.J. Lovón-Quintana, G.I. Almerindo, G.P. Valença, M.I.B. Bernardi, V.D. Araújo, T.S. Rodrigues, P.A. Robles-Dutenhefner, H.V. Fajardo, Preparation, structural characterization and catalytic properties f Co/CeO_2 catalysts for the steam reforming of ethanol and hydrogen production, J. Power Sources 216 (2012) 281–289.
[51] S.M. De Lima, A.M. Da Silva, L.O.O. Da Costa, U.M. Graham, G. Jacobs, B.H. Davis, L.V. Mattos, F.B. Noronha, Study of catalyst deactivation and reaction mechanism of stem reforming, partial oxidation, and oxidative stem reforming of ethanol over Co/CeO_2 catalyst, J. Catal. 268 (2009) 268–281.
[52] A.C. Ferrari, J. Robertson, Resonant Raman spectroscopy of disordered, amorphous, and diamond like carbon, Phys. Rev. B 64 (2001), 075414.